In situ X-ray diffraction of silicate liquids and glasses under dynamic and static compression to megabar pressures

Guillaume Morard, Jean-Alexis Hernandez, Marco Guarguaglini, Riccardo Bolis, Alessandra Benuzzi-Mounaix, Tommaso Vinci, Guillaume Fiquet, Marzena A Baron, Sang Heon Shim, Byeongkwan Ko, et al.

In situ X-ray diffraction of silicate liquids and glasses under dynamic and static compression to megabar pressures

Guillaume Morard[a,b], Jean-Alexis Hernandez[c,d], Marco Guarguaglini[c], Riccardo Bolis[c], Alessandra Benuzzi-Mounaix[c], Tommaso Vinci[c], Guillaume Fiquet[a], Marzena. A. Baron[a], Sang Heon Shim[e], Byeongkwan Ko[e], Arianna E. Gleason[f,g], Wendy L. Mao[f], Roberto Alonso-Mori[g], Hae Ja Lee[g], Bob Nagler[g], Eric Galtier[g], Dimosthenis Sokaras[g], Siegfried H. Glenzer[g], Denis Andrault[h], Gaston Garbarino[i], Mohamed Mezouar[i], Anja K. Schuster[j] and Alessandra Ravasio[c]

[a] *Sorbonne Université, Institut de Minéralogie, de Physique des Matériaux et de Cosmochimie, IMPMC, Museum National d'Histoire Naturelle, UMR CNRS 7590, 4 Place Jussieu, 75005 Paris, France.*

[b] *Univ. Grenoble Alpes, Univ. Savoie Mont Blanc, CNRS, IRD, IFSTTAR, ISTerre, 38000 Grenoble, France*

[c] *Laboratoire pour l'Utilisation des Lasers Intenses (LULI), Ecole Polytechnique, CNRS, CEA, UPMC, 91128 Palaiseau, France*

[d] *Center for Earth Evolution and Dynamics, University of Oslo, Norway*

[e] *School of Earth and Space Exploration, Arizona State University, Tempe, Arizona, USA*

[f] *Geological Sciences, Stanford University, Stanford, CA, USA*

[g] *SLAC National Accelerator Laboratory, 2575 Sand Hill Road, Menlo Park, CA 94025, USA*

[h] *Université Clermont Auvergne, CNRS, IRD, OPGC, LMV, Clermont-Ferrand, France*

[i] *European Synchrotron Radiation Facility, ESRF, Grenoble, France*

[j] *Helmholtz-Zentrum Dresden Rossendorf, Bauztner Landstr. 400, D-01328 Dresden, Germany*

Abstract

Properties of liquid silicates under high pressure and high temperature conditions are critical for modeling the dynamics and solidification mechanisms of the magma ocean in the early Earth, as well as for constraining entrainment of melts in the mantle and in the present-day core-mantle boundary. Here, we present *in situ* structural measurements by X-ray diffraction of selected amorphous silicates compressed statically in diamond anvil cells (up to 157 GPa at room temperature) or dynamically by laser-generated shock compression (up to 130 GPa and 6000 K along the $MgSiO_3$ glass Hugoniot). The X-ray diffraction patterns of silicate glasses and liquids reveal similar characteristics over a wide pressure and temperature range. Beyond the increase in Si coordination observed at 20 GPa, we find no evidence for major structural changes occurring in the silicate melts studied up to pressures and temperatures exceeding Earth's core mantle boundary conditions. This result is supported by molecular dynamics calculations. Our

findings reinforce the widely-used assumption that the silicate glasses studies are appropriate structural analogs for understanding the atomic arrangement of silicate liquids at these high pressures.

Significance

Understanding the structural changes silicate melts undergo over the pressure-temperature range of the Earth's mantle has been a major, longstanding challenge in the geosciences. Experimental studies are extremely difficult, due to required temperatures exceeding 4000 K needed to melt silicates over megabar pressures. To overcome this issue, novel laser-driven shock experiments combined with X-ray Free-Electron Lasers were performed to provide nanosecond resolution on silicate structural transformations. By comparison with statically compressed diamond-anvil cell experiments at ambient temperature, a common high-pressure structural evolution of glasses and liquid silicates was revealed. This supports the concept that silicate glasses of dominant mantle composition are suitable structural analogues for the corresponding liquids at these pressures.

Main text

Introduction

Terrestrial planet interiors have silicate-based mantles and iron-rich cores. It is generally accepted that this structure is inherited from early differentiation stages occurring in concert with radiogenic decay of short-lived nuclides and multiple shock events inducing temperatures high enough to sustain a global magma ocean. Hence, the physical properties of liquid silicates over a wide pressure-temperature range are crucial for understanding early differentiation events that occurred in Earth and other rocky planets (1). Those properties, especially the density, control the extent over which silicate melts can be stably entrained in the mantle (2). In addition, liquid silicates exist in our present-day upper mantle (3–5) and potentially at the core-mantle boundary (CMB) (6, 7). The exact composition and origin of molten or partially-molten domains in the deep mantle remain enigmatic. Direct measurements of molten mantle material properties to relevant pressures and temperatures are required to constrain these geodynamic processes (8, 9) as well as candidate materials contributing to mantle heterogeneities (10).

$MgSiO_3$ is the end member composition for the most abundant mineral of the Earth's mantle, i.e. bridgmanite (11). Liquid $MgSiO_3$ is arguably the closest proxy for liquid silicates in deep Earth. Its simple chemical composition includes two important features of liquid silicates at ambient pressure, with SiO_4 building blocks and octahedral Mg cation sites. In crystalline $MgSiO_3$, the pressure-induced transition to bridgmanite above 23 GPa is accompanied by an increase in coordination, from 4- to 6-fold, of Si sites by O atoms. Such dramatic atomic reorganization may also affect the properties of the corresponding liquid (12, 13).

The experimental study of liquid $MgSiO_3$ has been a long-term challenge, as $MgSiO_3$ melts at extremely high temperatures even at moderate pressures (melting temperature exceeds 4000 K at 40 GPa (14–16)). Therefore, $MgSiO_3$ glass has been extensively studied as a possible structural analog for the liquid state at high pressures (13, 17–19). Vibrational spectroscopy identified structural changes (13, 19–21) which were confirmed by *in situ* X-ray diffraction (XRD) studies (22, 23). This led to early constraints on the density of mantle melts at CMB conditions (18). However, the validity of the liquid/glass structural analogy has been a longstanding question. In order to probe lattice-level structural changes of liquid silicates, XRD from laser-driven shock compression with nanosecond resolution were collected with femtosecond X-ray pulses from a Free Electron Laser. These results were compared to static compression experiments and Molecular Dynamics simulations.

Results

We performed *in situ* XRD measurements on three silicate glasses: $MgSiO_3$, $Mg_3Si_2O_7$, and SiO_2. XRD patterns were collected up to 160 GPa at room temperature under static compression using diamond-anvil cells (DACs) and up to 130 GPa and ~6000 K under dynamic compression. Dynamic compression experiments reached the liquid phase along the principal Hugoniot. Integrated XRD patterns for $MgSiO_3$ glasses measured under dynamic and static compression, as well as synthetic spectra obtained from molecular dynamics (MD) simulations, are shown in Figure 1. Similar features were observed for these different approaches as well as for previous results from large volume experiments (17) (Figure 1). Amorphous $MgSiO_3$ displays a first large diffuse feature at 20 nm^{-1} (Q1) below a few GPa; this is clearly visible in the static compression data at 2.9 GPa, while in the dynamic experiment reference spectrum Q1 is mixed with the signal from the unshocked polystyrene ablator at lower Q-values (Figure 1). The signal from the ablator disappears upon shock compression and the recorded patterns capture contributions from both the shocked and

unshocked parts due to experimental geometry. Careful background subtraction allows the separation of these two contributions (SI Appendix, Figure S2). A second diffuse diffraction peak (Q2) arises under compression in both static and dynamic data around Q-values of 30-35 nm^{-1} (Figure 1) (17, 24) and marks the transition towards a dense amorphous structure. This spectral evolution is related to the transition from 4- to 6-fold oxygen coordination around the Si atoms (17, 24). As the pressure is further increased, both diffuse scattering peaks shift toward higher Q. The relative intensity of the second (Q2) compared to the first peak (Q1) increases, as qualitatively illustrated by intensity plots (Figure 1) and quantitatively confirmed by the structure factors S(Q) (SI Appendix, Figure S3).

Shock-compressed $MgSiO_3$ glass does not show evidence for recrystallization at the nanosecond timescale up to 129(±35) GPa and 6000 K, well above the melting along the Hugoniot (SI Appendix, Figure S5). This observation highlights a fundamental difference with fused silica SiO_2 which is found to crystallize into stishovite in a few- to 100s of nanoseconds (25, 26) under shock compression. The absence of recrystallization of $MgSiO_3$ glass along the Hugoniot may be related to the presence of Mg affecting the degree of polymerization, thus leading to an increased stability of the glass structure at nanosecond timescales. The dense disordered structures obtained in both static and dynamic compressions can therefore be compared along the entire pressure range reached in the shock experiment, which includes equilibrium liquid conditions. Indeed, according to previous works, melting of $MgSiO_3$ glass samples along the principal Hugoniot is expected to occur between 90 and 110 GPa (15, 16) (SI Appendix, Figure S5). In our dynamic experiments, we used velocimetry records via a velocity interferometer system for any reflector (VISAR) diagnostic to determine the peak pressure in our shots. Four out of the six datasets presented in Figure 1 can be assigned to pressures below 90 GPa, considering the existing measurements of the Hugoniot of liquid $MgSiO_3$ from shocked $MgSiO_3$ glass (15, 16, 27–29) and the Hugoniot of $MgSiO_3$ glass as calculated from density functional theory (DFT) MD simulations (30), and are therefore in a glassy solid state. The two data points at 124 and 129 GPa are above the melting curve and are representative of a high-pressure liquid (SI Appendix, Figure S5). To a first approximation, the data show no significant difference between the diffraction of the glass acquired along the Hugoniot and the corresponding liquid at similar pressure conditions.

The limited Q range available for dynamic compression XRD patterns precludes a more detailed analysis, specifically preventing a real space analysis of the diffraction patterns. This limitation was intrinsic to the experimental setup available (see Methods). The partial structure factors for $MgSiO_3$ glass highlight the fact that this portion of the total structure

factor is mainly related to contributions from cation-anion (Mg-O and Si-O) bonds (22, 31). A further consequence of the limited Q-range intrinsic to the dynamic experiments is the inability to accurately track structural differences between statically and dynamically compressed samples at the atomic level. However, differences in atomic arrangements should be reflected in a change in the structure factor, with the appearance of new diffuse peaks (e.g. between 2.5 and 20 GPa in Figure 1) or by a difference in the Q1/Q2 ratio. In this regard, we find that the XRD signal obtained from shock compression of $MgSiO_3$ glasses follows the same Q1/Q2 trend as the one from DAC-compressed glasses (Figure 2). Moreover, another silicate glass with an Mg-enriched composition ($Mg_3Si_2O_7$) also follows a similar Q1/Q2 trend (Figure 2, SI Appendix, Figure S7). Our experiment also provides evidence that liquid SiO_2 has a similar structure because the Q1/Q2 ratio lies on the trend found for statically compressed SiO_2 glass (Figure 2). The difference in absolute position of the two features of amorphous MgSiO3 and SiO2 samples can be attributed to the presence of Mg. Based on this data, it can be stated that silicate glasses at high pressures and room temperature have remarkably similar structures to their corresponding liquids at high temperatures. In addition, no modification of the amorphous structure with increasing SiO2 content (from 50% ($MgSiO_3$) to 60% ($Mg_3Si_2O_7$)) was observed, which agrees with reported results of glasses at ambient pressure (32).

The pressure dependence of the first sharp diffraction peak (FSDP) Q1 is often used as a proxy for pressure induced changes in coordination number (33–36). For example, correlation between pressure increase in Q1 and evolution of oxygen-packing fraction is a common feature for a large variety of glasses (33). Figure 3 illustrates the Q1 dependence on pressure for our data, without evidence for sharp discontinuities in both the liquids and glasses, indicating monotonic structural changes (24) with increasing pressure up to the liquid state. In particular, the MD simulations (see Methods for details) reproduce the correlation between Q1 and Q2 values found in our experiment, for both intensity distribution (Figure 1) and quantitative Q1/Q2 ratios (Figure 2). The simulations show a correlation between Q1 and Q2 values very similar to the experimental one, and the coordination number of O around Si smoothly increases from 6 to 7 (between 6.1 and 6.7; SI Appendix, Table S8).

It is challenging to discriminate between temperature effects and structural rearrangements, when comparing the pressure dependent peak positions of Q1 and Q2 under static compression at room temperature and dynamic compression along the Hugoniot. Therefore, peak positions are also plotted as a function of density (Figure 3 and 4). For static compression, density values were extracted from recent experimental studies of amorphous

SiO2 and MgSiO3 (18, 37). For dynamic compression, they were deduced from VISAR measurements and a known equation of state (see Methods). The error propagation involved in this analysis results in large uncertainties (up to 30%) for the density of the shocked state. The plots clearly show no significant difference in peak position between statically compressed glass and high temperature disordered silicates with similar densities, suggesting that no structural changes occur over the entire examined density range. This analysis can be extended to the second diffraction peak Q2, which appears above 10 GPa (Figure 4). Theoretical calculations (31), indicate that Q2 is related to the evolution of cation-anion bonds and the appearance of 5- and 6-fold coordinated Si-O and Mg-O polyhedra. The pressure dependence of the Q2 position is similar for dynamic and static compression. Moreover, the SiO_2 and $MgSiO_3$ samples show comparable Q2 features as a function of pressure, suggesting similar packing mechanisms.

Conclusions

Dynamic compression experiments allowed us to probe the structure of liquid silicates with compositions relevant to the Earth's lower mantle (over 130 GPa and 6000 K). Although the limited Q range does not allow for a full structural description, no evidence for major structural changes between liquid and cold compressed silicate glass was found. In particular, the ratio of Q1/Q2 measured for cold compressed $MgSiO_3$ glass at 90 GPa and room temperature is very similar to that of liquid $MgSiO_3$ along the Hugoniot at 130 GPa and 6000 K. Similar conclusions can be drown for liquid and statically compressed SiO_2. Therefore, XRD measurements of cold compressed silicate glasses can be used to infer structural properties of liquid silicates at Earth's interior conditions. Our experiments further demonstrate the possibility of high-quality XRD diffraction measurements of liquid silicates to previously inaccessible pressure-temperature regimes. In addition, signatures of chemical reactions between the shocked liquids and the target chamber are minimized in the *in situ* XRD spectra due to the nanosecond timescale of the shock compression experiment (or the femtosecond probing timescale of the XFEL) (38).

The absence of major structural change under pressure up to ~130 GPa in liquid $MgSiO_3$ is expected to be important for modeling partial melts at depth in the Earth. Similar mechanisms are likely to occur in rocky exoplanets with Earth-like compositions (39). Finally, our results indicate that combined static and dynamic datasets could be used to infer silicate liquid properties. Future dynamic compression experiments combined with XFEL

sources are complementary tools suitable for probing liquid silicates under extreme conditions.

Methods

Target preparation and characterization

Targets for shock compression consisted of a 50 µm-thick polystyrene ablator glued to a silicate sample (between 35 to 90 µm thickness) that was polished on both sides, and coated with 300 nm Ti on the drive laser side prior to gluing (SI Appendix, Figure S9). Glass starting materials with $MgSiO_3$ and $Mg_3Si_2O_7$ compositions were synthetized by laser levitation in an inert gas flux of argon. Fused silica starting material was manufactured by Asphera company. The thickness of each sample as well as its planarity were individually measured using a 2D interferometer. This characterization has been used for a relevant estimate of the mean shock velocity and hence of the induced pressure.

Static compression

$MgSiO_3$ glass was synthetized by laser levitation of $MgSiO_3$ powder in an inert gas flow of Ar. Flakes of the glass were placed in a pre-indented and drilled Re gasket. For the lower pressure (LP) run, a gas driven membrane Le Toullec type DAC was used to compress the sample up to 100 GPa. A small piece of KCl was placed on the side of the sample in order to calculate pressure from the equation of state (EoS) (40). The experimental setup available on the High Pressure beamline ID27 (ESRF, Grenoble, France) (41) included KB mirrors to focus the X-ray beam to 3x3 μm^2, a MAR CCD detector to collect the diffraction pattern, and a multichannel collimator slit system to reduce the inelastic X-ray contribution from the diamond anvils (42, 43). High-quality data were obtained with this set-up, enabling the extraction of a high Q range structure factor (SI Appendix, Figure S3).

The background contribution from the diamond anvils was first measured by placing an empty DAC in the X-ray beam. Then the background was subtracted from the sample diffraction patterns. The diffraction was normalized to obtain the structure factor S(Q) following the previously described method (44, 45). For the high pressure (HP) run up to 160 GPa, a different experimental setup was used (SI Appendix, Figure S4). The background from the diamonds was collected on the empty cell and removed from the raw signal. The Re-gasket EoS was used to determine the pressure, which is well correlated with the EoS of KCl used in the LP run (46).

Dynamic compression

High pressure and temperature conditions in the $MgSiO_3$ glass samples were obtained via laser-driven shock compression using the two frequency-doubled Nd-glass laser beams available at the Matter in Extreme Conditions (MEC) end-station of the Linac Coherent Light Source (LCLS) at SLAC National Acceleratory Laboratory. Various thermodynamic conditions could be generated by choosing the laser energy for a 10ns square pulse on a 250um focal spot, smoothed using a continuous phase plate.

In situ XRD measurements were performed using quasi-monochromatic (dE/E = 0.2−0.5%), 9.0 keV X-ray pulses of 60 fs duration with an average of ~ 10^{12} photons per pulse. The LCLS X-ray free electron laser spot size was set to 50 μm diameter, much smaller than the flat compressed region so as to avoid detecting pressure and temperature gradients. The measurement of uniform thermodynamic conditions during shock propagation were ensured by optimizing the target design and probe timing. Example patterns collected on the CSPADs of the typical diffuse scattering of amorphous silicates under high pressures and temperatures are shown in SI Appendix, Figure S8. The accessible energy and position of the CSPAD were limited at the MEC end-station at the time of the experiment.

The time-resolved velocity of the reflecting interfaces in the sample were measured by two Doppler interferometers (VISARs) operating at 532 nm whose VPF were 4.658 km/s and 1.814 km/s. For most of the targets, time-resolved particle velocity inside the sample could be measured from the VISAR fringe shift if the sample remained transparent after shock loading. The mean shock velocity inside the sample was instead measured from the shock arrival and exit times recorded on the VISAR images. For some of the targets, the time-resolved material velocity inside the rear-side lithium fluoride window was also measured to investigate the shock stationarity.

The shock pressure was deduced by inserting the measured shock and particle velocities into the Rankine-Hugoniot equations, in case they were recorded. For the shots where only the shock velocity could be measured, the known principal Hugoniot curves (fused silica (SESAME 7386), $MgSiO_3$ glass (27, 29)) were used to estimate the pressure. An independent pressure estimate could be obtained by applying the impedance matching technique between the sample and the lithium fluoride window. SESAME 7270 was used extract the lithium fluoride Hugoniot curve. The uncertainties on pressure estimates were determined via a Monte-Carlo routine which repeated the analysis 5000 times. Each analysis was performed extracting the inputs from a Gaussian distribution whose mean were the

measured value and the standard deviation were the estimated uncertainty. The standard deviation of the output distribution has been taken as the uncertainty in pressure. An extensive discussion on the VISAR analysis is presented in the Supplementary information.

Molecular dynamics simulations

MD simulations were performed using the LAMMPS code (47). Pair potentials constructed in Oganov et al. 2000 (48) were used to model the interactions between Mg, Si and O atoms. The simulations contained a total of 112000 atoms and were performed in the isobaric-isothermal (NPT) ensemble with a time step of 1 fs. The first melt structure was created by heating an orthoenstatite structure at ambient pressure up to 4000 K, and equilibrating the resulting melt during 100 ps. Then, we compressed and heated the system to the target pressure-temperature conditions in 100 ps (SI Appendix, Table S6). The cells were then equilibrated during an additional 100 ps at the considered high pressure-temperature conditions. XRD intensities were then calculated using the USER-DIFFRACTION package implemented in LAMMPS (49).

Data availability

The different data presented in this manuscript are available in the Supplementary Information.

Acknowledgements

The authors would like to thank F. Lefèvre, N. Coudurier and B. Baptiste for their help with target characterization and preparation and B. Guillot for fruitful discussions. G. Morard, G. Fiquet and M. A. Baron acknowledge funding from the European Research Council (ERC) under the European Union's Horizon 2020 Research and Innovation program (ERC PlanetDive; grant agreement No 670787). A. E. Gleason acknowledges the LANL Reines LDRD. A. Gleason and W. Mao acknowledge support from the NSF Geophysics Program (EAR0738873). A.K.S. is supported by the Helmholtz Association under VH-NG-1141. This research was also supported by the POMPEI program of the Agence National de la Recherche (Grant ANR-16-CE31-0008). Dynamic compression experiments were performed at the MEC instrument of LCLS, supported by the U.S. DOE Office of Science, Fusion Energy Science under contract No. SF00515, FWP 100182, and was supported by LCLS, a National User Facility operated by Stanford University on behalf of the U.S. DOE, Office of Basic Energy Sciences. Static compression experiments were performed on ID27 beamline at ESRF.

References

1. Elkins-Tanton LT (2012) Magma Oceans in the Inner Solar System. *Annu Rev Earth Planet Sci* 40(1):113–139.
2. Labrosse S, Hernlund JW, Coltice N (2007) A crystallizing dense magma ocean at the base of the Earth's mantle. *Nature* 450(7171):866–869.
3. Sanloup C (2016) Density of magmas at depth. *Chem Geol* 429:51–59.
4. Schmandt B, Jacobsen SD, Becker TW, Liu Z, Dueker KG (2014) Dehydration melting at the top of the lower mantle. *Science (80-)* 344(6189):1265–1268.
5. Tauzin B, Debayle E, Wittlinger G (2010) Seismic evidence for a global low-velocity layer within the Earth ' s upper mantle. *Nat Geosci* 3(10):718–721.
6. Lay T, Williams Q, Garnero EJ (1998) The core–mantle boundary layer and deep Earth dynamics. *Nature* 392(2):461–468.
7. Fiquet G, et al. (2010) Melting of peridotite to 140 gigapascals. *Science* 329(5998):1516–1518.
8. Wen L, Helmberger D V (1998) Ultra-Low Velocity Zones Near the Core-Mantle Boundary from Broadband PKP Precursors. *Science* 279(March):1701–1704.
9. Garnero EJ, McNamara AK, Shim S-H (2016) Continent-sized anomalous zones with low seismic velocity at the base of Earth's mantle. *Nat Geosci* 9(June):481.
10. Trønnes RG, et al. (2019) Tectonophysics Core formation , mantle differentiation and core-mantle interaction within Earth and the terrestrial planets. *Tectonophysics* (October 2018):1–34.
11. Tschauner O, Beckett JR, Prescher C, Prakapenka VB, Rossman GR (2014) Discovery of bridgmanite, the most abundant mineral in Earth, in a shocked meteorite. *Science* 346(6213):1100–1103.
12. Stixrude L, Karki B (2005) Structure and Freezing of MgSiO 3 Liquid in Earth ' s Lower Mantle. *Science* 185(October):297–300.
13. Murakami M, Bass JD (2011) Evidence of denser MgSiO3 glass above 133 gigapascal (GPa) and implications for remnants of ultradense silicate melt from a deep magma ocean. *Proc Natl Acad Sci* 108(42):17286–17289.
14. Shen G, Lazor P (1995) Measurement of melting temperatures of some minerals under lower mantle pressures. *J Geophys Res* 100(B9):17699–17713.
15. Akins JA, Luo SN, Asimow PD, Ahrens TJ (2004) Shock-induced melting of MgSiO3 perovskite and implications for melts in Earth's lowermost mantle. *Geophys Res Lett*

31(14):2–5.

16. Mosenfelder JL, Asimow PD, Frost DJ, Rubie DC, Ahrens TJ (2009) The MgSiO3system at high pressure: Thermodynamic properties of perovskite, postperovskite, and melt from global inversion of shock and static compression data. *J Geophys Res Solid Earth* 114(1):1–16.

17. Kono Y, Shibazaki Y, Kenney-Benson C, Wang Y, Shen G (2018) Pressure-induced structural change in $MgSiO_3$ glass at pressures near the Earth's core–mantle boundary. *Proc Natl Acad Sci*:201716748.

18. Petitgirard S, et al. (2015) Fate of $MgSiO_3$ melts at core–mantle boundary conditions. *Proc Natl Acad Sci* 112(46):14186–14190.

19. Sanchez-Valle C, Bass JD (2010) Elasticity and pressure-induced structural changes in vitreous MgSiO3-enstatite to lower mantle pressures. *Earth Planet Sci Lett* 295(3–4):523–530.

20. Shim S, Catalli K (2009) Compositional dependence of structural transition pressures in amorphous phases with mantle-related compositions. *Earth Planet Sci Lett* 283(1–4):174–180.

21. Kubicki JD, Hemley RJ, Hofmeister AM (1992) Raman and infrared study of pressure-induced structural changes in MgSiO3 CaMgSi2O6, and CaSiO3 glasses. *Am Mineral* 77:258–269.

22. Wilding MC, Benmore CJ, Tangeman JA, Sampath S (2004) Coordination changes in magnesium silicate glasses. *Europhys Lett* 67(2):212–218.

23. Cormier L, Cuello GJ (2013) Structural investigation of glasses along the MgSiO3-CaSiO3join: Diffraction studies. *Geochim Cosmochim Acta* 122(December):498–510.

24. Prescher C, et al. (2017) Beyond sixfold coordinated Si in SiO_2 glass at ultrahigh pressures. *Proc Natl Acad Sci*:201708882.

25. Gleason AE, et al. (2017) Time-resolved diffraction of shock-released SiO2and diaplectic glass formation. *Nat Commun* 8(1):8–13.

26. Gleason AE, et al. (2015) Ultrafast visualization of crystallization and grain growth in shock-compressed SiO2. *Nat Commun* 6:1–6.

27. Luo SN, Akins JA, Ahrens TJ, Asimow PD (2004) Shock-compressed MgSiO3 glass, enstatite, olivine, and quartz: Optical emission, temperatures, and melting. *J Geophys Res Solid Earth* 109(5):1–14.

28. Spaulding DK, et al. (2012) Evidence for a phase transition in silicate melt at extreme pressure and temperature conditions. *Phys Rev Lett* 108(6):1–4.

29. Bolis RM, et al. (2016) Decaying shock studies of phase transitions in MgO-SiO2 systems: Implications for the super-Earths' interiors. *Geophys Res Lett* 43(18):9475–9483.
30. de Koker N, Stixrude L (2009) Self-consistent thermodynamic description of silicate liquids, with application to shock melting of MgO periclase and MgSiO3 perovskite. *Geophys J Int* 178(1):162–179.
31. Ghosh DB, Karki BB, Stixrude L (2014) First-principles molecular dynamics simulations of MgSiO 3 glass : Structure , density , and elasticity at high pressure. *Am Mineral* 99:1304–1314.
32. Wilding MC, Benmore CJ, Tangeman JA, Sampath S (2004) Evidence of different structures in magnesium silicate liquids: Coordination changes in forsterite- to enstatite-composition glasses. *Chem Geol* 213(1–3):281–291.
33. Zeidler A, Salmon PS (2016) Pressure-driven transformation of the ordering in amorphous network-forming materials. *Phys Rev B* 93(21):1–5.
34. Meade C, Hemley RJ, Mao HK (1992) High-Pressure X-Ray Diffraction of Si02 Glass. *Phys Rev Lett* 69(9):1387–1391.
35. Benmore CJ, et al. (2011) High pressure x-ray diffraction measurements on Mg2SiO 4 glass. *J Non Cryst Solids* 357(14):2632–2636.
36. Sato T, Funamori N (2008) Sixfold-Coordinated Amorphous Polymorph of SiO2 under High Pressure. *Phys Rev Lett* 101(25):255502.
37. Petitgirard S, et al. (2017) SiO2 Glass Density to Lower-Mantle Pressures. *Phys Rev Lett* 119(November):215701.
38. Morard G, et al. (2018) Solving controversies on the iron phase diagram under high pressure. *Geophys Res Lett* 45:1–9.
39. Stixrude L (2014) Melting in super-earths. *Philos Trans R Soc A* 372(March):20130076.
40. Dewaele A, et al. (2012) High-pressure-high-temperature equation of state of KCl and KBr. *Phys Rev B - Condens Matter Mater Phys* 85(21):1–7.
41. Mezouar M, et al. (2005) Development of a new state-of-the-art beamline optimized for monochromatic single-crystal and powder X-ray diffraction under extreme conditions at the ESRF. *J Synchrotron Radiat* 12(5):659–664.
42. Morard G, et al. (2011) High efficiency multichannel collimator for structural studies of liquids and low-Z materials at high pressures and temperatures. *Rev Sci Instrum* 82(2):2–7.

43. Weck G, et al. (2013) Use of a multichannel collimator for structural investigation of low-Z dense liquids in a diamond anvil cell: Validation on fluid H2 up to 5 GPa. *Rev Sci Instrum* 84(6).
44. Eggert J, Weck G, Loubeyre P, Mezouar M (2002) Quantitative structure factor and density measurements of high-pressure fluids in diamond anvil cells by x-ray diffraction: Argon and water. *Phys Rev B* 65(17):1–12.
45. Morard G, et al. (2014) Density measurements and structural properties of liquid and amorphous metals under high pressure. *High Press Res* 34(1).
46. Anzellini S, Dewaele A, Occelli F, Loubeyre P, Mezouar M (2014) Equation of state of rhenium and application for ultra high pressure calibration. *J Appl Phys* 115(4).
47. Plimpton S (1995) Fast parallel algorithms for short range molecular dynamics. *J Comput Phys* 117:1–19.
48. Oganov AR, Brodholt JP, Price GD (2000) Comparative study of quasiharmonic lattice dynamics , molecular dynamics and Debye model applied to MgSiO3 perovskite. *Phys Earth Planet Int* 122:277–288.
49. Coleman SP, Spearot DE, Capolungo L (2013) Virtual diffraction analysis of Ni [0 1 0] symmetric tilt. *Model Simul Mater Sci Eng*:055020.
50. Militzer B (2013) Ab initio investigation of a possible liquid-liquid phase transition in MgSiO3 at megabar pressures. *High Energy Density Phys* 9(1):152–157.
51. Fratanduono DE, et al. (2018) Thermodynamic properties of MgSiO3 at super-Earth mantle conditions. *Phys Rev B* 97(21):214105.

Figure Captions

Figure 1: **Diffraction patterns of compressed amorphous $MgSiO_3$ obtained under static and dynamic compression, and from molecular dynamics simulations.** Top left: XRD patterns for $MgSiO_3$ glass collected during static compression in a DAC. Full S(Q), up to 80 nm^{-1}, are presented in SI Appendix, Figure S3. Diffraction patterns for $MgSiO_3$ up to 160 GPa are presented in SI Appendix, Figure S4. Top right: XRD patterns collected for $MgSiO_3$ amorphous targets compressed along the Hugoniot during dynamic compression experiments. The reported pressures, hence the liquid or glassy solid state of the sample, are determined from VISAR measurements (see Supplementary Materials). Diffraction peaks around 24 and 28 nm^{-1} come from the shocked Ti layer located between the ablator and the sample (see SI Appendix, Figure S1). The signal from the cold part of the sample has been removed following the procedure presented in Figure S2. There is a clear evolution toward higher Q-values for the two main sample contributions (Q1 and Q2). Bottom left: XRD patterns calculated from MD simulations. Details for the calculations are given in the Methods section. Different pressure-temperature conditions are presented in SI Appendix, Figure S5, corresponding to two Hugoniots representing extreme cases (50, 51). Bottom right: Comparison of different XRD patterns at similar density, 4.5 $g.cm^{-3}$. The XRD patterns collected in a previous large volume experiment have been recalculated from the dataset presented (17). The dashed vertical lines serve as guides for the eyes.

Figure 2: Correlation between First (Q1) and Second (Q2) Diffraction peaks for $MgSiO_3$, $Mg_3Si_2O_7$, and SiO_2 glasses under static and dynamic compression (SI Appendix, Tables S1-S6). Round symbols represent data acquired during static compression using DACs ($MgSiO_3$ glass: with multichannel collimator (MCC) experimental set-up (43) (black circles) and without (red circles); SiO_2 glass: data from literature (24, 34)). Square symbols represent diffraction experiments recorded during dynamic compression (starting with SiO_2 glass, $MgSiO_3$ glass, $Mg_3Si_2O_7$ glass, and $MgSiO_3$ enstatite crystals). In addition, results from our MD simulations of $MgSiO_3$ glass are shown as filled blue diamonds.

Figure 3: Position of the first sharp diffraction peak (FSDP) Q1 for $MgSiO_3$ and SiO_2 compressed amorphous samples as a function of density (SI Appendix, Tables S1-S6). Density of cold compressed glasses is calculated following recent experimental measurements (18, 37). Density of shocked samples is calculated following VISAR measurements (see

463 Methods). Round, square and diamond symbols are similar to Figure 2. Inset: peak position as
464 a function of pressure. Pressures for shock compressed samples are calculated from VISAR
465 measurements (see Methods).
466
467 **Figure 4: Position of the second diffraction peak (Q2) for $MgSiO_3$ and SiO_2 compressed**
468 **amorphous samples as a function of density (SI Appendix, Tables S1-S6).** This second
469 peak appears in the diffraction pattern above 10 GPa. Symbols used in this figure are similar
470 to those in Figure 3. Inset: peak position as a function of pressure, following the method used
471 in Figure 3.
472

Static cold compression

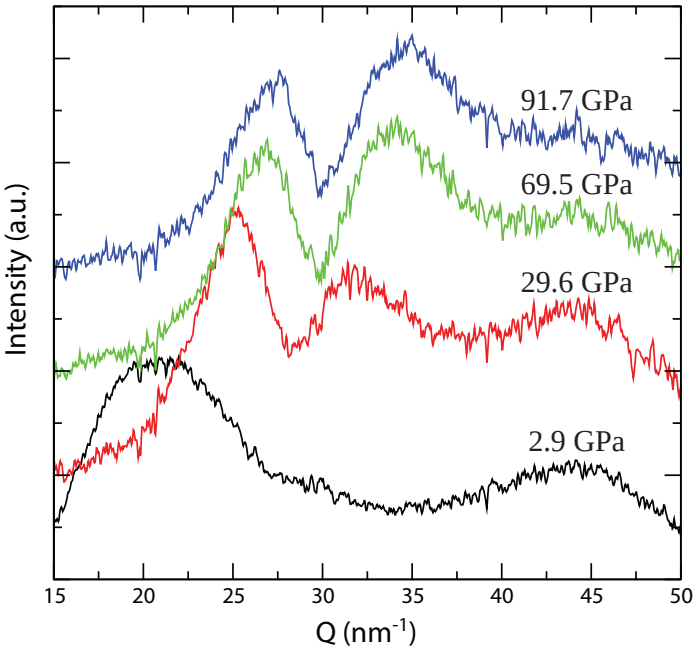

Dynamic compression

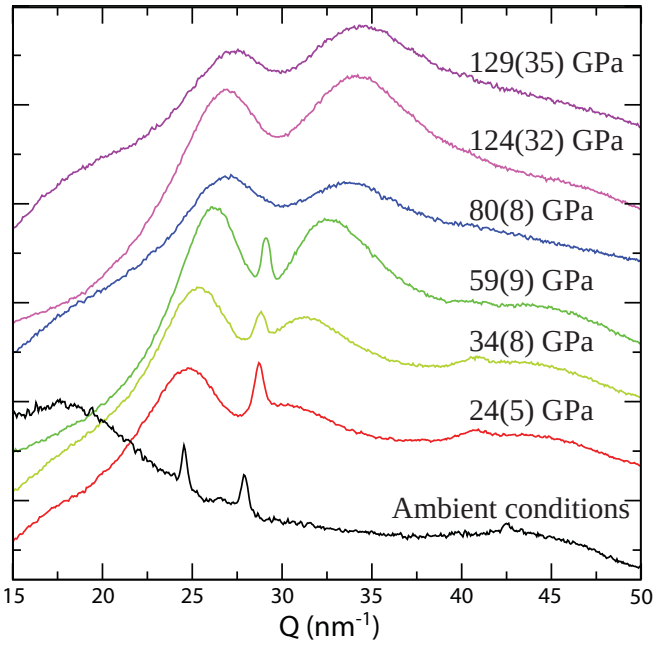

Molecular dynamics

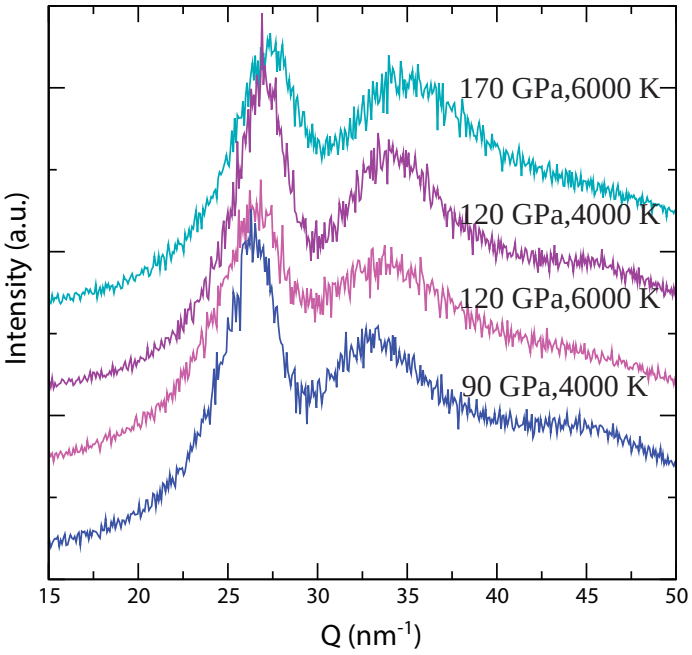

Comparison at similar density

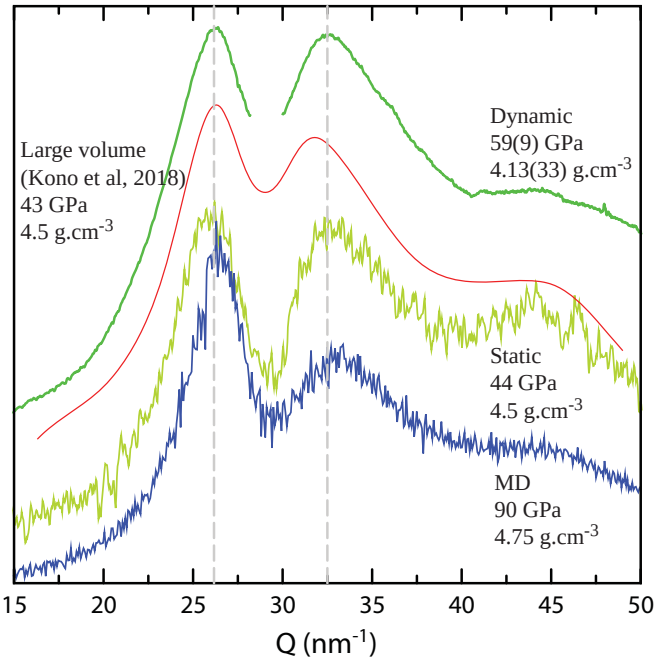

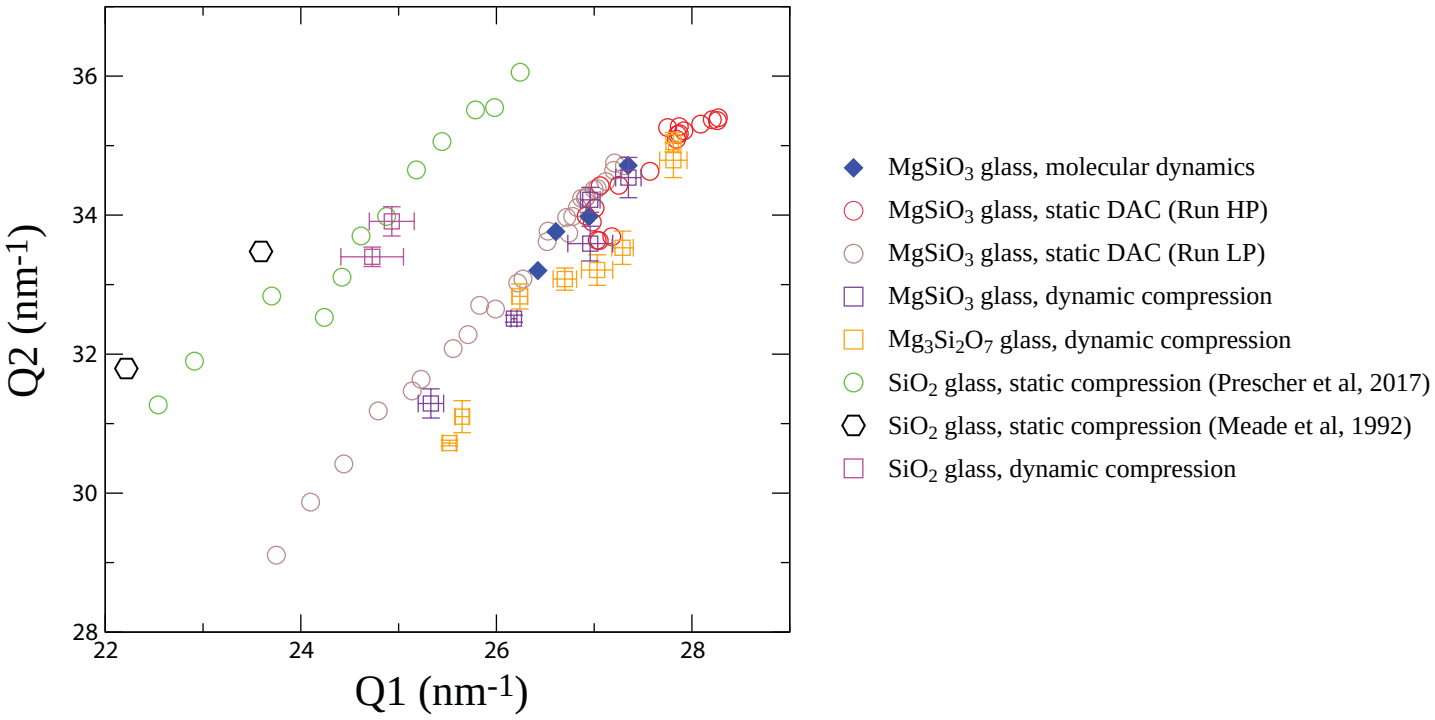
36
34
32
30
28
22
24
26
28
Q2 (nm-1)
Q1 (nm-1)
MgSiO3 glass, molecular dynamics
MgSiO3 glass, static DAC (Run HP)
MgSiO3 glass, static DAC (Run LP)
MgSiO3 glass, dynamic compression
Mg3Si2O7 glass, dynamic compression
SiO2 glass, static compression (Prescher et al, 2017)
SiO2 glass, static compression (Meade et al, 1992)
SiO2 glass, dynamic compression

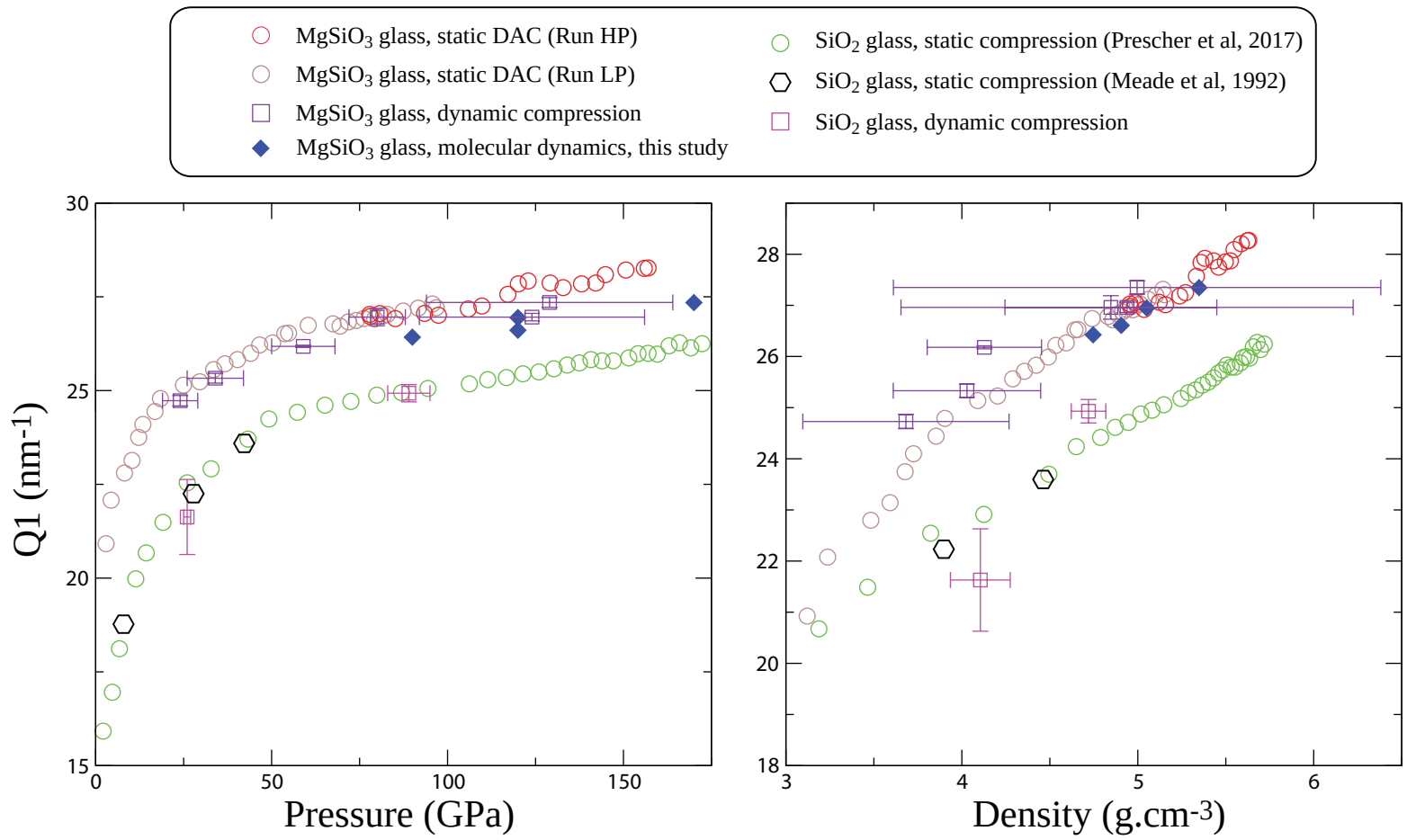
MgSiO3 glass, static DAC (Run HP)
MgSiO3 glass, static DAC (Run LP)
MgSiO3 glass, dynamic compression
MgSiO3 glass, molecular dynamics, this study
SiO2 glass, static compression (Prescher et al, 2017)
SiO2 glass, static compression (Meade et al, 1992)
SiO2 glass, dynamic compression
Q1 (nm-1)
Pressure (GPa)
Density (g.cm-3)

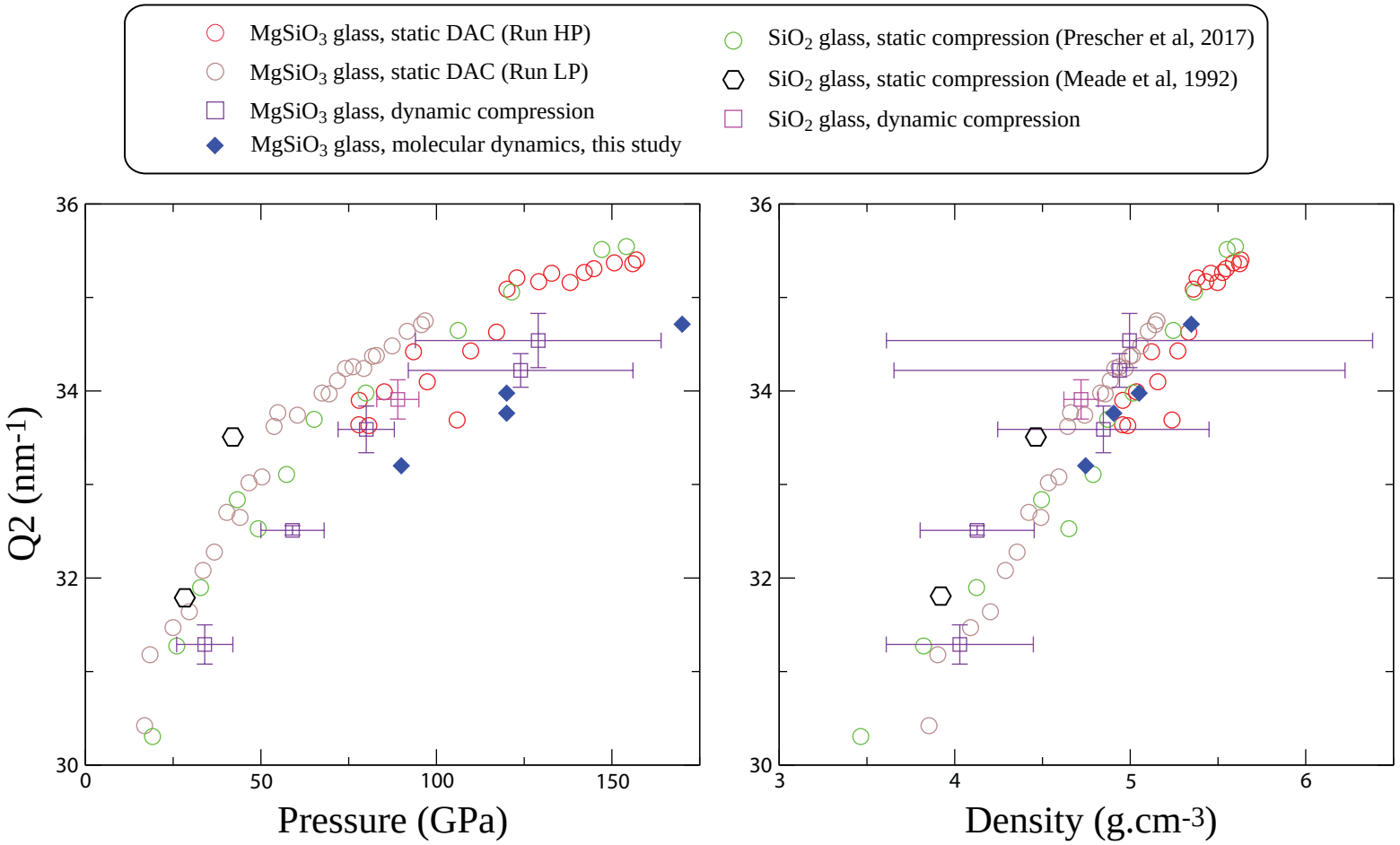
MgSiO3 glass, static DAC (Run HP)
MgSiO3 glass, static DAC (Run LP)
MgSiO3 glass, dynamic compression
MgSiO3 glass, molecular dynamics, this study
SiO2 glass, static compression (Prescher et al, 2017)
SiO2 glass, static compression (Meade et al, 1992)
SiO2 glass, dynamic compression
Q2 (nm-1)
Pressure (GPa)
Density (g.cm-3)
30
32
34
36
0
50
100
150
3
4
5
6